Coupling of two-dimensional atomistic and continuum models for dynamic crack*

Ren Guo-Wu(任国武)† and Tang Tie-Gang(汤铁钢)

Institute of Fluid Physics, China Academy of Engineering Physics, Mianyang 621900, *China*

(Received 19 May 2014; revised manuscript received 6 June 2014; published online 24 September 2014)

A concurrent multiscale method of coupling atomistic and continuum models is presented in the two-dimensional system. The atomistic region is governed by molecular dynamics while the continuum region is represented by constructing the mass and stiffness matrix dependent on the coarsening of the grids, which ensures that they merge seamlessly. The low-pass phonon filter embedded in the handshaking region is utilized to effectively eliminate the spurious reflection of high-frequency phonons, while keeping the low-frequency phonons transparent. These schemes are demonstrated by numerically calculating the reflection and transmission coefficient, and by the further application of dynamic crack propagation subjected to mode-I tensile loading.

Keywords: concurrent multiscale method, phonon filter, dynamic crack

PACS: 87.15.ap, 62.20.mm, 63.20.–e **DOI:** 10.1088/1674-1056/23/11/118704

1. Introduction

Multiscale modelling enables us to study the properties of strongly coupled system spanning over a wide range of length and time scale, such as fracture and turbulence. Generally, the concurrent multiscale methods integrate different physical models, such as, atomic scale described by density-functional theory or empirical interatomic potential and macro scale by continuum constitutive relation. In the last few decades, numerous multiscale methods have been proposed to couple atomistic and continuum length scales,[1] such as coupling of length scales (CLS) method,[2,3] quasicontinuum (QC) method,[4–6] coarse-grained molecular dynamics (CGMD),[7,8] bridge scale method (BSM),[9,10] and coupled atomistic and discrete dislocation (CADD) method.[11] The common feature of these multiscale methods is that they allow for exact treatment of the critical region and general description of the far-field region with small deformation. To date, significant progress have been devoted to investigating the mechanical process of materials, such as fracture[12,13] and contact.[14]

However, due to the physical discrepancy of coupling between two length scales, the existence of such an atomistic-continuum interface inevitably causes spurious phonon reflection, which interferes with the dynamics in the atomistic region and prevents the multiscale method from simulating dynamical properties. A previous study[15] has indicated that spurious wave reflection occurs at the nonuniform grid of finite element region. Recently, several approaches have been employed to eliminate this reflection, such as stadium boundary condition (BC),[16,17] exact boundary condition,[18–21] and absorbing BC[22] or perfectly matched layer (PML).[23,24] The introduction of these BCs by adopting either a time-dependent or position dependent damping term effectively dampens all of the waves near the interface region.

Considering the different physical properties of two coupled models, the low-frequency phonon can freely travel back and forth through the interface region, while the high-frequency phonon can only exist in the atomic region. Meanwhile, the low-frequency phonon plays a significant role in understanding the long range interaction related to mechanical deformation. Hence, the boundary conditions should be frequency dependent and transmit the phonon of the frequency as high as possible. The previously proposed BCs either are difficult to perform because they involve the computation of convolution integrals[19] or they dampen all of the phonons[17] nearby the coupled interface. Therefore, it is essential to construct an appropriate algorithm to dynamically couple the atomistic and continuum modelling.

The phenomenon under consideration in this paper is the dynamic crack propagation[25,26] imposed by mode-I tensile loading, which involves an evident pressure wave radiating from the crack tip. The stress wave propagates outward to the boundary of the simulation domain and reflects back towards the central domain. The present goal of the multiscale method is to allow such pressure waves in the atomistic region to propagate harmlessly into the continuum region. The early multiscale methods[2,4,11] have been only applied for the static or quasistatic case without taking into account elastic wave effect.

This work is an extension of the previously developed

*Project supported by the National Natural Science Foundation of China (Grants Nos. 11102191 and 11172279) and the Development Foundation of Institute of Fluid Physics, Chinese Academy of Engineering Physics (Grant No. SFZ20120402).

†Corresponding author. E-mail: guowu.ren@gmail.com

© 2014 Chinese Physical Society and IOP Publishing Ltd

multiscale method in the one-dimensional modelling[27] to the two-dimensional (2D) case. In what follows, an atomic-based finite element method (AFEM) is theoretically derived for the continuum region, which can be merged seamlessly with molecular dynamics (MD) in the atomistic region. We also utilize the low-pass phonon filter[27] to eliminate the spurious reflection of longitudinal and transverse phonons induced by the varying mesh-size grid, while keeping the transmission of low-frequency phonons. Numerical results demonstrate the effectiveness of these schemes by calculating the reflection and transmission coefficient. We also apply this multiscale method to investigate the dynamic crack propagation under mode-I tensile loading.

2. Theoretical method and analysis

We consider a 2D multiscale model which spatially consists of an MD region, FE region and linking region (LR), as displayed in Fig. 1. Lagrangian mechanics are adopted to describe the MD region, in the absence of external force, which is given by

$$L(\boldsymbol{u},\dot{\boldsymbol{u}}) = \frac{1}{2}\dot{\boldsymbol{u}}^{\mathrm{T}}\boldsymbol{M}_{\mathrm{A}}\dot{\boldsymbol{u}} - V(\boldsymbol{u}), \tag{1}$$

where $\boldsymbol{M}_{\mathrm{A}}$ is diagonal mass matrix denoted by atomic mass m_μ, and $V(\boldsymbol{u})$ is the short-ranged interatomic potential. The displacement vector is $\boldsymbol{u} = \boldsymbol{r} - \boldsymbol{r}_0$, where $\boldsymbol{r}$ and $\boldsymbol{r}_0$ are the deformed and reference position, respectively. The dynamics of atoms can be obtained by numerically integrating the Newton's law of motion derived from the Lagrangian equation, expressed as

$$m_\mu \ddot{\boldsymbol{r}}_\mu = -\frac{\partial V(\boldsymbol{r}_\mu)}{\partial \boldsymbol{r}_\mu}. \tag{2}$$

For the sake of simplicity, we choose a square lattice for MD region. With the introduction of initial position and velocity, the dynamical trajectories of the atoms can be determined. On the basis of statistical analysis, macroscopic physical quantity can be calculated, such as temperature by averaging the kinetic energy of atoms.

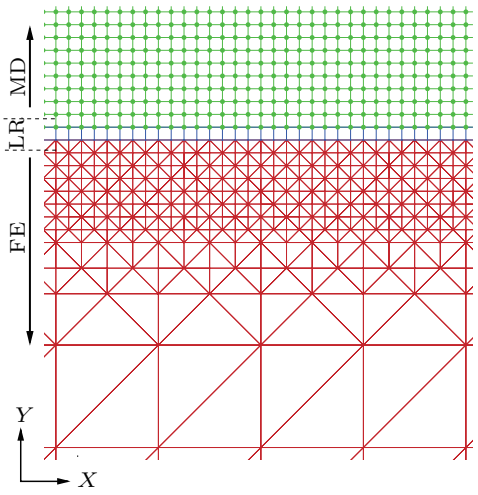


Fig. 1. (color online) Schematic of a two-dimensional multiscale model that includes the MD region, FE region, and linking region (LR).

Since the conventional FE method is derived from the macroscale continuum constitutive mechanics, the atomic behavior representing localized bond and discrete mass could not be captured. Although the lumped mass approximation[2,3] is chosen to match with the discrete distribution of atomic mass, this approximation conflicts with the consistent distribution of mass in the continuous region, which can be greatly improved.

The FE region is divided into triangular elements, which are generated by adaptive mesh refinement bisecting the longest edge, as can be seen from FE part of Fig. 1. It should be noted that the nodes need to coincide with the atomic sites, where the densest elements located at the interface region require a direct atom-node correspondence and mesh length is gradually scaled up away the atomic region. Under the kinematic constraint condition, the atomic displacement $\boldsymbol{u}$ is the linear mapping of the nodal displacement $\boldsymbol{d}$, expressed as, $\boldsymbol{u} = \boldsymbol{N}d$, where $\boldsymbol{N}$ is the Jacobi matrix of the linear interpolation function which provides the atomic displacement within the element. By substituting this relation into Eq. (1), and by solving the corresponding Lagrangian equation, the equation of motion can be written as

$$[\boldsymbol{M}][\ddot{\boldsymbol{d}}] = -[\boldsymbol{K}][\boldsymbol{d}], \tag{3}$$

where $[\boldsymbol{M}] = \boldsymbol{N}^{\mathrm{T}}[\boldsymbol{M}]_{\mathrm{A}}\boldsymbol{N}$ is the mass matrix, and $[\boldsymbol{K}] = \partial^2 V(\boldsymbol{N}d)/\partial \boldsymbol{d}^2$ is the stiffness matrix.

In terms of the divided principle of elements, a concrete formula about mass and stiffness matrix can be obtained. For the lth mesh, the local mass matrix is given by

$$[\boldsymbol{M}]^l = \sum_\mu m_\mu [N]^{\mathrm{T}}[N], \tag{4}$$

with

$$[N] = \left[N_i(\boldsymbol{r}_{0\mu})I \;\; N_j(\boldsymbol{r}_{0\mu})I \;\; N_k(\boldsymbol{r}_{0\mu})I\right],$$

where N_i, N_j, and N_k are the linear interpolation functions at nodes i, j, and k, and $\boldsymbol{I}$ is the two-dimensional identity matrix.

The area coordinate is utilized to evaluate the interpolation function at the initial position. In light of the definition of the area coordinate, for any atomic sites P_μ inside the element, N_i, N_j, and N_k are separately dependent on the area of $\Delta P_\mu jk$, $\Delta P_\mu ki$, and $\Delta P_\mu ij$, as shown in Fig. 2, where the length of right-angle side of triangular element is h_1. Hence, the area S_{ijk} of Δijk is $h_1^2/2$, and the area $S_{P_\mu jk}$, $S_{P_\mu ki}$, and $S_{P_\mu ij}$ of $\Delta P_\mu jk$, $\Delta P_\mu ki$, and $\Delta P_\mu ij$ are $(h_1^2 - ta_\mu h_1 - sa_\mu h_1)/2$, $sa_\mu h_1/2$, and $ta_\mu h_1/2$, respectively, where a_μ is the equilibrium lattice constant. The integers s and t denote the atomic index along the horizontal and vertical direction. Defining the total length

ratio $n_1 = h_1/a_\mu$, the interpolation function N_i, N_j, and N_k can be rewritten as

$$N_i = \frac{n_1 - s - t}{n_1};\ N_j = \frac{s}{n_1};\ N_k = \frac{t}{n_1}, \tag{5}$$

where the value of s and t is from 0 to n_1. Thus, in terms of Eq. (5), all of the values of interpolation function corresponding to the atomic sites within the element can be obtained. Note that the interpolation function is normalized and local on the mesh nodes, suggesting that at this node its value is 1 and goes linearly to zero at the nearest-neighbor nodes.

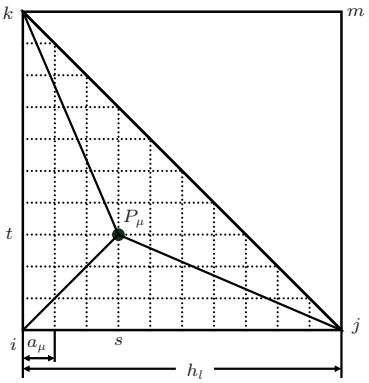


Fig. 2. Schematic illustration of distribution of atomic sites within the element.

In Fig. 2, all of the atomic sites distribute at the edge, vertex, and inner of the triangle. Using Eqs. (4) and (5), the expression of local mass matrix can be derived as

$$[\boldsymbol{M}]^l = \begin{bmatrix} m^l_\alpha & 0 & m^l_\gamma & 0 & m^l_\gamma & 0 \\ 0 & m^l_\alpha & 0 & m^l_\gamma & 0 & m^l_\gamma \\ m^l_\gamma & 0 & m^l_\beta & 0 & m^l_\gamma & 0 \\ 0 & m^l_\gamma & 0 & m^l_\beta & 0 & m^l_\gamma \\ m^l_\gamma & 0 & m^l_\gamma & 0 & m^l_\beta & 0 \\ 0 & m^l_\gamma & 0 & m^l_\gamma & 0 & m^l_\beta \end{bmatrix}, \tag{6}$$

where

$$m^l_\alpha = m_\mu \frac{n_1^2+2}{12};\ m^l_\beta = m_\mu \frac{2n_1^2+1}{24};\ m^l_\gamma = m_\mu \frac{n_1^2-1}{24}.$$

Accordingly, the global mass matrix is constructed to be $[\boldsymbol{M}] = \sum_l [M]^l$.

The local stiffness matrix of the l-th mesh is represented as

$$\boldsymbol{K}^l_{ij} = \sum_\mu \frac{\partial^2 V(\boldsymbol{r}_\mu)}{\partial \boldsymbol{d}^l_i \partial \boldsymbol{d}^l_j}, \tag{7}$$

where $\boldsymbol{d}^l_i$ is the component of the node i. To obtain the analytic form of stiffness matrix $\boldsymbol{K}^l_{ij}$, we only consider the nearest neighbor and the second nearest neighbor interaction described by harmonic potential,

$$\begin{aligned} V(\boldsymbol{r}_\mu) =\ & \frac{1}{2} f_1 \sum_{\mu,\delta_1} (|\boldsymbol{r}_\mu - \boldsymbol{R}_{\mu+\delta_1}| - a_\mu)^2 \\ & + \frac{1}{2} f_2 \sum_{\mu,\delta_2} (|\boldsymbol{r}_\mu - \boldsymbol{R}_{\mu+\delta_2}| - \sqrt{2} a_\mu)^2, \end{aligned} \tag{8}$$

where $\delta_1 = (\pm a_\mu, 0), (0, \pm a_\mu)$ and $\delta_2 = (\pm a_\mu, \pm a_\mu)$ are the interaction sites; and, f_1 and f_2 are the force constant of the nearest neighbor and second nearest neighbor interaction, respectively.

For the element of Fig. 2, the atomic displacement field can be expressed by

$$\boldsymbol{u}_{P_\mu} = N_i \boldsymbol{d}_i + N_j \boldsymbol{d}_j + N_k \boldsymbol{d}_k = \frac{n_1 - s - t}{n_1} \boldsymbol{d}_i + \frac{s}{n_1} \boldsymbol{d}_j + \frac{t}{n_1} \boldsymbol{d}_k. \tag{9}$$

Combining Eqs. (8) and (9) into Eq. (7) yields the following stiffness matrix:

$$[\boldsymbol{K}]^l = \begin{bmatrix} -\left(\frac{f_1}{2} + \frac{2n_1-1}{2n_1} f_2\right) & -\frac{2n_1-1}{2n_1} f_2 & \frac{f_1}{2} + \frac{n_1-1}{2n_1} f_2 & \frac{n_1-1}{2n_1} f_2 & \frac{n_1-1}{2n_1} f_2 & \frac{n_1-1}{2n_1} f_2 & \frac{f_2}{2n_1} & \frac{f_2}{2n_1} \\ -\frac{2n_1-1}{2n_1} f_2 & -\left(\frac{f_1}{2} + \frac{2n_1-1}{2n_1} f_2\right) & \frac{n_1-1}{2n_1} f_2 & \frac{n_1-1}{2n_1} f_2 & \frac{n_1-1}{2n_1} f_2 & \frac{f_1}{2} + \frac{n_1-1}{2n_1} f_2 & \frac{f_2}{2n_1} & \frac{f_2}{2n_1} \\ \frac{f_1}{2} + \frac{n_1-1}{2n_1} f_2 & \frac{n_1-1}{2n_1} f_2 & -\left(\frac{f_1}{2} + \frac{2n_1-1}{4n_1} f_2\right) & \frac{f_2}{4n_1} & \frac{f_2}{4n_1} & -\frac{2n_1-1}{4n_1} f_2 & 0 & 0 \\ \frac{n_1-1}{2n_1} f_2 & \frac{n_1-1}{2n_1} f_2 & \frac{f_2}{4n_1} & -\frac{2n_1-1}{4n_1} f_2 & -\frac{2n_1-1}{4n_1} f_2 & \frac{f_2}{4n_1} & 0 & 0 \\ \frac{n_1-1}{2n_1} f_2 & \frac{n_1-1}{2n_1} f_2 & \frac{f_2}{4n_1} & -\frac{2n_1-1}{4n_1} f_2 & -\frac{2n_1-1}{4n_1} f_2 & \frac{f_2}{4n_1} & 0 & 0 \\ \frac{n_1-1}{2n_1} f_2 & \frac{f_1}{2} + \frac{n_1-1}{2n_1} f_2 & -\frac{2n_1-1}{4n_1} f_2 & \frac{f_2}{4n_1} & \frac{f_2}{4n_1} & -\left(\frac{f_1}{2} + \frac{2n_1-1}{4n_1} f_2\right) & 0 & 0 \end{bmatrix}. \tag{10}$$

As can be seen from Eq. (10), the stiffness matrix is completely distinguishable from that of the conventional FE method.[28] Except for the regular interaction among the nodes i, j, and k, it also involves the additional interaction between nodes i and m, shown in the rightmost two columns of Eq. (10), resulting from the second neighbor interaction of atomic model. It should be mentioned that there are three other types of triangular element that counterclockwise rotate by $\pi/4$, $\pi/2$, and $3\pi/4$ relative to element of Fig. 2 (see Appendix A). The corresponding stiffness matrix must be theoret-

ically derived in great detail and has a similar interaction form as discussed above. Eventually, the global stiffness matrix is assembled by $[\boldsymbol{K}] = \sum_l [\boldsymbol{K}]^l$.

Hereto we have obtained the equation of the AFEM model, which is comprised by mesh-dependent mass and stiffness matrix together, as shown in Eqs. (6) and (6). When the element length equals with lattice constant as $n_l = 1$, the mass matrix will be reduced to a diagonal and the equation of AFEM is corresponding with that of the MD region. For $n_l = \infty$, the mass and stiffness matrix tends toward the consistent distribution of conventional FE case,[28] as calculated by

$$[\boldsymbol{K}]^l = \frac{1}{4S}[\boldsymbol{B}]^{\mathrm{T}}[\boldsymbol{C}][\boldsymbol{B}], \tag{11}$$

where $[\boldsymbol{B}]$ is related to the nodal coordinate, S is the area of the element l, and $[\boldsymbol{C}]$ is elastic constant matrix determined by atomic potential

$$[\boldsymbol{C}] = \begin{bmatrix} f_1 + f_2 & f_2 & 0 \\ f_2 & f_1 + f_2 & 0 \\ 0 & 0 & f_2 \end{bmatrix}. \tag{12}$$

The case of $n_l = \infty$ exhibits the continuous feature. Therefore, it can be concluded that the present equation of AFEM can seamlessly extend from atomic scale to continuous scale.

3. Simulation results

In this section, we perform a dynamical simulation in the 2D multiscale model, as depicted in Fig. 1. The FE grid is adaptively refined to scale down to the atomic spacing as $n_l = 1$ and maximum value of element length n_l is up to 8. In the finest FE region nearby the interface, the equation of the AFEM model is equivalent to that of the MD region, so that there is no spurious reflection at the atomistic/continuum interface, which is better than the previous linking methods.[3] The Gaussian wave packet initially located in the MD region is employed to simulate the dynamics of wave propagation traveling from the MD region to the FE region along the Y direction.

During the simulation process, the velocity Verlet algorithm is used for time integration with a fixed time step for the whole system. The mass and stiffness matrix of FE region must be globally assembled prior to the simulation and then the nodal accelerations in the time iteration procedure are solved by preconditioned conjugate gradient method. The central wave vector of the wave packet is determined from the phonon dispersion curve of two-dimensional atomic model, including the longitudinal and transverse modes, in which the maximum frequencies are $\omega_{\mathrm{L}} = 2\sqrt{(f_1 + f_2)/m_\mu}$ and $\omega_{\mathrm{T}} = 2\sqrt{f_2/m_\mu}$, respectively. In the practical simulation, f_1 and f_2 are separately chosen to be 300.0 and 150.0, indicating that the simulated system corresponds to an isotropic elastic body. The lattice constant and atomic mass is set to be 1 and the reduced time step is chosen to be 0.003, ensuring the numerical stability. The X direction is treated as a periodic boundary condition for the overall coupled system.

3.1. Damping analysis

As stated previously, spurious reflection unavoidably generates because the short-wavelength modes cannot be supported by the larger mesh spacing inherent in the FE region and are scattered back into the MD region, which leads to the thermal nonequilibrium with an increase of local temperature. Analogue to the one-dimensional case, we apply the developed phonon filter (PF) method[27] to absorb the reflected phonons larger than the cutoff frequency related to the mesh length n_l,

$$m_\nu \ddot{u}_\nu = -\frac{\partial V(u_\nu)}{\partial u_\nu} + \beta(\dot{u}_{\nu+1} + \dot{u}_{\nu-1} - 2\dot{u}_\nu), \tag{13}$$

which involves the two-order difference of the velocity between neighbor atoms, replacing the damping term proportional to the on-site velocity in the Langevin dynamics. This damping form depends on the vibrated frequency. Note that the parameter β is the key for effectively absorbing the spurious phonon reflection and if it is too large β will cause overdamping. Multiple low-pass filter layers roughly estimating the damping width are placed nearby the handshaking region.

Figure 3 represents the results of longitudinal phonon for three different simulation methods: lumped mass FE method, AFEM without any damping scheme, AFEM with PF method, as shown in Figs. 3(a)–3(c), respectively. The wave packet with central wave vector $K_y = 0.1(\pi/32)$ and $K_y = 11(\pi/32)$ are chosen for testing. For $K_y = 0.1(\pi/32)$, there is a significant phonon reflection using the lumped mass FE method; however, for the AFEM, the wave-packet is essentially transmitted. For $K_y = 11(\pi/32)$, the wave packet is completely reflected, and nothing can propagate toward the FE region for the lumped mass FE method and AFEM. But after using the PF method, the spurious reflection is completely damped out as desired.

By calculating the energy change between MD and FE region, we numerically obtain the dependence of reflection and transmission coefficient on vibrated frequency. Figure 4 shows the reflection and transmission coefficient, which is plotted as a function of frequency ω for three different simulation conditions. The results show that AFEM with PF method can eliminate the spurious reflection of high-frequency phonon and have very little influence on transmission of low-frequency phonon, but the lumped mass FE method remains as a strong reflection. Meanwhile, it is observed that the AFEM has a lower reflection coefficient than the lumped mass FE method. From the reflection coefficient, one can see that most of the spurious reflections are damped out and only a small fraction of frequencies near $\omega = 10$ exists because the transfer function is not optimal like the perfect filter.

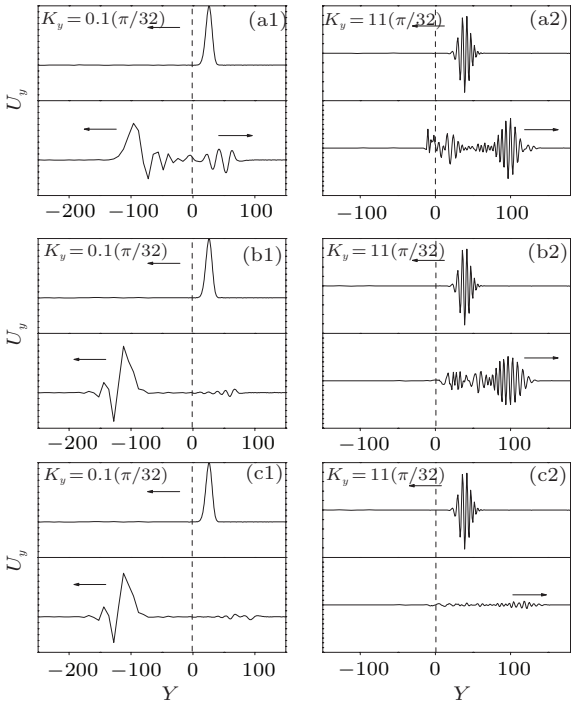


Fig. 3. Gaussian wave packet of small wave vector (left column) and large wave vector (right column) for longitudinal phonon propagates from MD region to FE region: (a) lumped mass FE method; (b) AFEM; (c) AFEM with PF method. The dashed line denotes the coupled interface corresponding to the $Y = 0$ axis. The use of AFEM improves the transmission of small wave vector. Additionally, it is clear that AFEM with PF method has little effect on the small wave vector packet, while dampening the large wave vector packet.

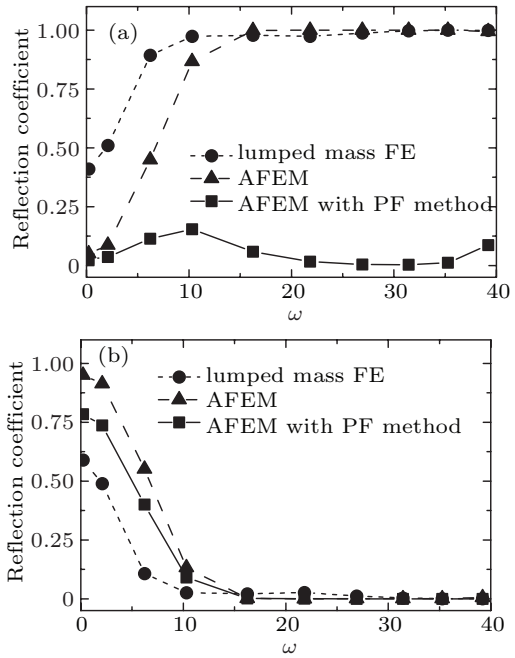


Fig. 4. A comparison of (a) reflection and (b) transmission coefficient for longitudinal phonon is shown using the lumped mass FE method, AFEM, and AFEM with PF method.

Similar simulations are performed for the transverse phonon, where figure 5 shows the propagation with the wave packet of wave vector $K_y = 0.1(\pi/32)$ and $K_y = 11(\pi/32)$ using the three different simulation approaches: lumped mass FE method, AFEM without any damping scheme, AFEM with PF method. Compared to the three simulation results, the AFEM with PF method can entirely reduce the refection of wave packet with $K_y = 11(\pi/32)$, while keeping the transmission of wave packet with $K_y = 0.1(\pi/32)$. The corresponding reflection and transmission coefficient as a function of frequency is displayed in Fig. 6, indicating that a large majority of phonon reflections are eliminated, while the low-frequency phonons are almost unchanged using AFEM with the PF method.

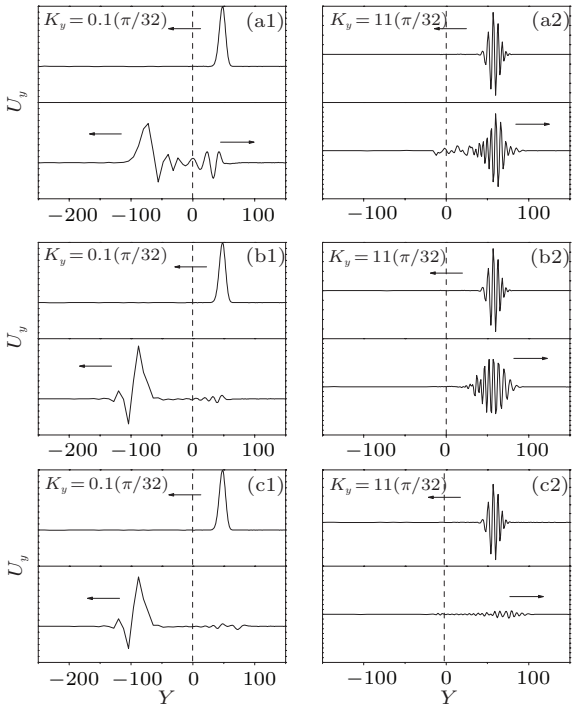


Fig. 5. The dynamics of a Gaussian wave packet of small and large wave vector is for transverse phonon: (a) lumped mass FE method; (b) AFEM; (c) AFEM with PF method. It is evident that AFEM with PF method makes the wave packet of small wave vector transparent, while damping the wave packet of the large wave vector.

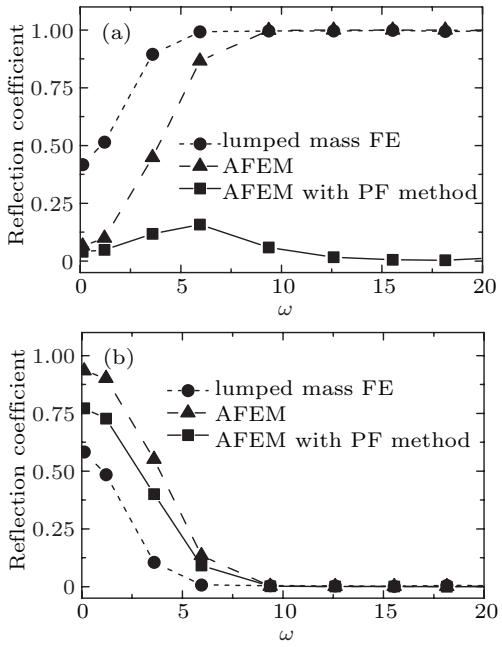


Fig. 6. (a) Reflection and (b) transmission coefficients for transverse phonon are shown as plots of wave frequencies.

3.2. Dynamic crack simulation

Dynamic crack propagation is a complicated process spanning the multiple length and time scale, and involves the complex pressure wave effect. Here our aim is to demonstrate the effectiveness of the above developed multiscale approach through the simple simulation of rapid fracture process. A sharp triangular precrack is created at the top edge of atomistic region away from non-uniform finite element region and its length is about one-fourth the size of the atomic region. Figure 7 displays the multiscale model of a crack system, divided by three parts: atomistic region, handshaking region and continuum region. The mesh size in the vicinity of FE region close to atomistic region is densest in that length is equal to the atomic distance, and the mesh gradually increases up to the largest length in the outer boundary of the FE region.

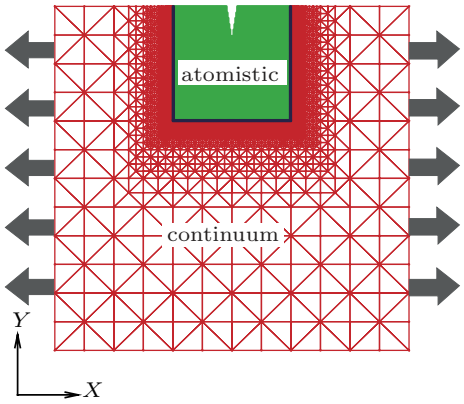


Fig. 7. (color online) Multiscale model of a precrack subjected to mode-I tensile loading.

In the simulation process, it should be mentioned that all of the parameters are expressed by reduced units. The multiscale model only contains the degrees of freedom with about 10000 atoms and 500 nodes. The size of whole slap is 384×384, and the ratio of maximum mesh length to atomic distance is 32. The uniaxial tensile loading with a prescribed constant strain rate for mode-I crack is imposed at the oppositely outer boundary of FE region. A linear velocity gradient was applied along the X direction to avoid the wave reflection of the lateral boundary. The crack-tip position is determined by searching the surface atoms in the vicinity of the crack-tip region on the basis of choosing an appropriate threshold value of the potential energy. By numerically differentiating the position changing with time, an instantaneous crack-tip velocity can be obtained. Averaging over a small time interval can eliminate the unnecessary high-frequency fluctuation and improve the accuracy.

Calculated from the potentials (8) and (12) of the description of multi-particle interaction, the longitudinal and shear wave about elastic body are separately $c_{\mathrm{l}} = 21.21$ and $c_{\mathrm{s}} = 12.25$, and thus the Rayleigh wave speed c_{R} is about 11.39. To implement the simulation of the fracture, the multi-particle interaction potential is set to the finite bond extension u_{bc}. Once the atomic bond stretches to a distance lager than u_{bc}, the force between two particles drops to zero and never interacts again, such as brittle glass. The crack-tip position and velocity as a function of time are presented in Fig. 8. The imposed strain rate is 0.00042. Seen from this figure, at the reduced time about 18.9 with the critical strain for failure stretched by 7.9%, the crack starts to propagate and rapidly reaches a terminal velocity of $0.29c_{\mathrm{R}}$, where the acceleration process is smooth. However, after that the crack-tip velocity becomes unstable and has the onset of erratic fluctuation. Consequently the resulting limited velocity is about 0.35 of the Rayleigh speed, which is qualitatively consistent with the experimental observations of brittle glass and PMMA.[26] Figure 9 displays the schematic illustrations about the time evolution of the crack surface structure denoted by the transverse velocity v_x, where the process transitions from initiation to branching. A comparative observation between Figs. 8 and 9 shows that the onset of branching is corresponding with the fluctuation of crack-tip velocity. However, the characteristic of branching about this elastic body has only two son-cracks.

The boundary effect has a significant influence on crack propagation, particularly at the coupled interface of a multiscale model. Nevertheless, as seen from Fig. 9, there is no obvious reflection occurring at the linking region, which suggests that the multiscale methods composed of atomic-based finite element method and low-pass filter phonon method are very effective.

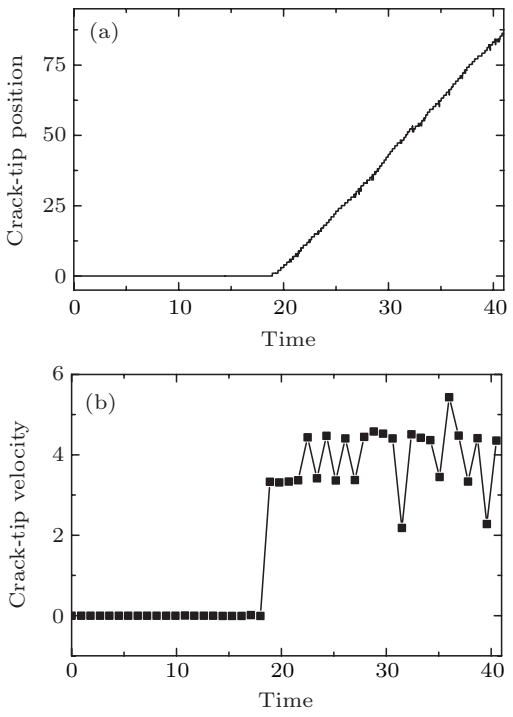


Fig. 8. History of (a) crack-tip position and (b) velocity.

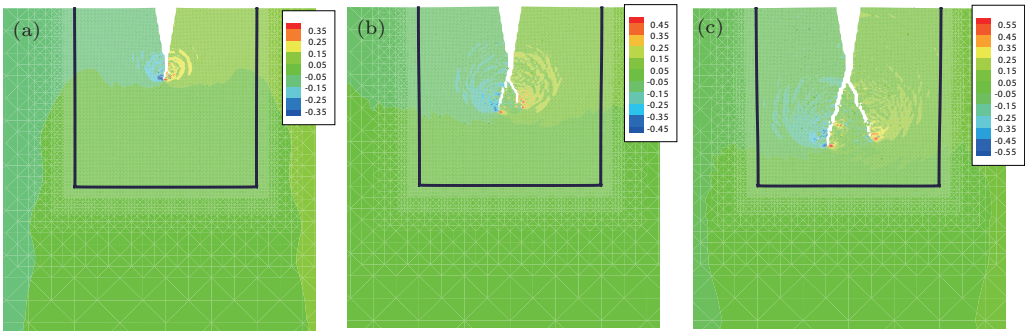


Fig. 9. (color online) Schematic close-up views of crack propagating (a)–(c) from initiation to branching.

4. Conclusions

In this paper, we have developed a concurrent multiscale algorithm by incorporating the equation of AFEM and PF method together in the 2D multiscale model. This multiscale method reveals some attractive advantages in comparison with the previous multiscale methods, as described in the introduction, such as QC and BSM. The latter are formulated on the basis of Cauchy–Born rule[29] in order to reduce the number degree of freedoms. The local approximative procedure for coarse-grid domain induces the QC method achieved by minimizing total energy and BSM by a least-squares fit. However, the AFEM used for continuum region completely retains the atomistic physical information by introducing the kinematic constraint, and thus realizes the seamless transition from atomic scale to continuum scale. The key is that it captures the atomistic information in the finest region, such as discrete mass distribution and nonlocal atomic bond interaction. For the numerous atoms within the large mesh, it yields the finite element representation of continuum mechanics. By applying this method, material properties from the atomistic region, in particular long-range interaction, will be transferred to the continuum region and generate more accurate results.

As for the utilization of the developed phonon filter method related to two-order difference of velocity, it can keep low-frequency phonons transparent and simultaneously dampen the reflection of high-frequency phonons. The effectiveness is validated by investigating the dynamics of a Gaussian wave packet, and the calculation of reflection and transmission coefficient. Physically, the phonon plays a significant role in the carrier of stress wave and thermal energy, which represent the low-frequency and high-frequency modes, respectively. The method aims at separating the total vibration modes of MD region into two parts, which are treated as mechanical and thermal energy in the continuum region. The low-frequency phonons associated with the mechanical effect should be maintained to transfer to the continuum region while the high-frequency ones that are not supported by the coarse mesh need be damped out. However, the latter carries the thermal energy for heat transport between MD and FE region, and should be gathered as a temperature boundary condition to couple with heat equation in the continuum system. Consequently, this method can achieve thermal and mechanical coupling, and it is also found that it is very easily implemented because of its simplicity. This is the subject of ongoing work.

For the further demonstration purpose, the present schemes is applied to simulate dynamic propagation of a brittle crack under mode-I tensile loading. By tracking the crack-tip velocity and observing the branching process, the results are reasonably consistent with the experimental findings. Finally, we can believe that the present hybrid methodology developed here can provide a promising application for dynamic phenomena at finite temperature.

Appendix A: Stiffness matrix of three other triangular elements

In this appendix, the three other types of triangular elements are displayed in Fig. 10. We ignore the detailed calculation of their mass matrices and only show the

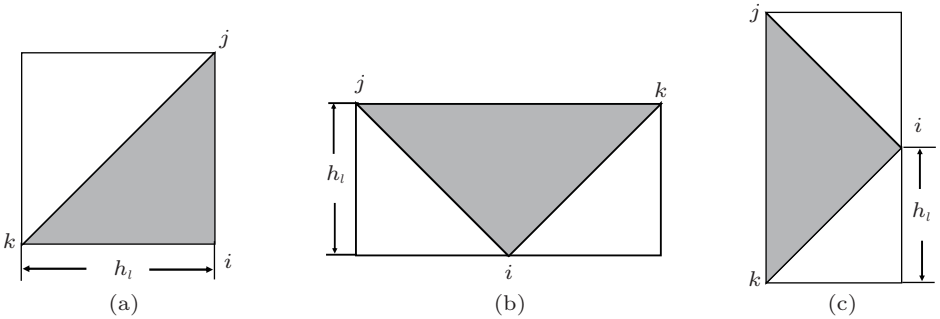


Fig. 10. Schematic of three other types of triangular elements.

results of stiffness matrices. The derived stiffness matrices of Figs. 10(a)–10(c) correspond to $[\boldsymbol{K}]_{\rm a}$, $[\boldsymbol{K}]_{\rm b}$, and $[\boldsymbol{K}]_{\rm c}$, respectively, where $n_{\rm l} = h_{\rm l}/a_\mu$, and f_1 are f_2 are the force constants. Compared to the stiffness matrix derived from the conventional FE method, it can be found that it is the result of AFEM model as $n_{\rm l}$ goes to infinity.

$$[\boldsymbol{K}]_{\rm a} = \begin{bmatrix}
-\left(\frac{f_1}{2}+\frac{2n_{\rm l}-1}{2n_{\rm l}}f_2\right) & \frac{2n_{\rm l}-1}{2n_{\rm l}}f_2 & \frac{n_{\rm l}-1}{2n_{\rm l}}f_2 & -\frac{n_{\rm l}-1}{2n_{\rm l}}f_2 & \frac{f_1}{2}+\frac{n_{\rm l}-1}{2n_{\rm l}}f_2 & -\frac{n_{\rm l}-1}{2n_{\rm l}}f_2 & \frac{f_2}{2n_{\rm l}} & -\frac{f_2}{2n_{\rm l}} \\
\frac{2n_{\rm l}-1}{2n_{\rm l}}f_2 & -\left(\frac{f_1}{2}+\frac{2n_{\rm l}-1}{2n_{\rm l}}f_2\right) & -\frac{n_{\rm l}-1}{2n_{\rm l}}f_2 & \frac{f_1}{2}+\frac{n_{\rm l}-1}{2n_{\rm l}}f_2 & -\frac{n_{\rm l}-1}{2n_{\rm l}}f_2 & \frac{n_{\rm l}-1}{2n_{\rm l}}f_2 & -\frac{f_2}{2n_{\rm l}} & \frac{f_2}{2n_{\rm l}} \\
\frac{n_{\rm l}-1}{2n_{\rm l}}f_2 & -\frac{n_{\rm l}-1}{2n_{\rm l}}f_2 & -\frac{2n_{\rm l}-1}{4n_{\rm l}}f_2 & -\frac{f_2}{4n_{\rm l}} & \frac{f_2}{4n_{\rm l}} & \frac{2n_{\rm l}-1}{4n_{\rm l}}f_2 & 0 & 0 \\
-\frac{n_{\rm l}-1}{2n_{\rm l}}f_2 & \frac{f_1}{2}+\frac{n_{\rm l}-1}{2n_{\rm l}}f_2 & -\frac{f_2}{4n_{\rm l}} & -\left(\frac{f_1}{2}+\frac{2n_{\rm l}-1}{4n_{\rm l}}f_2\right) & \frac{2n_{\rm l}-1}{4n_{\rm l}}f_2 & \frac{f_2}{4n_{\rm l}} & 0 & 0 \\
\frac{f_1}{2}+\frac{n_{\rm l}-1}{2n_{\rm l}}f_2 & -\frac{n_{\rm l}-1}{2n_{\rm l}}f_2 & \frac{f_2}{4n_{\rm l}} & \frac{2n_{\rm l}-1}{4n_{\rm l}}f_2 & -\left(\frac{f_1}{2}+\frac{2n_{\rm l}-1}{4n_{\rm l}}f_2\right) & -\frac{f_2}{4n_{\rm l}} & 0 & 0 \\
-\frac{n_{\rm l}-1}{2n_{\rm l}}f_2 & \frac{n_{\rm l}-1}{2n_{\rm l}}f_2 & \frac{2n_{\rm l}-1}{4n_{\rm l}}f_2 & \frac{f_2}{4n_{\rm l}} & -\frac{f_2}{4n_{\rm l}} & -\frac{2n_{\rm l}-1}{4n_{\rm l}}f_2 & 0 & 0
\end{bmatrix},$$

$$[\boldsymbol{K}]_{\rm b} = \begin{bmatrix}
-\frac{2n_{\rm l}-1}{2n_{\rm l}}f_2 & 0 & \frac{2n_{\rm l}-1}{4n_{\rm l}}f_2 & \frac{2n_{\rm l}-1}{4n_{\rm l}}f_2 & \frac{2n_{\rm l}-1}{4n_{\rm l}}f_2 & -\frac{2n_{\rm l}-1}{4n_{\rm l}}f_2 & 0 & 0 \\
0 & -(f_1+\frac{2n_{\rm l}-1}{2n_{\rm l}}f_2) & \frac{2n_{\rm l}-1}{4n_{\rm l}}f_2 & \frac{f_1}{2}+\frac{2n_{\rm l}-1}{4n_{\rm l}}f_2 & -\frac{2n_{\rm l}-1}{4n_{\rm l}}f_2 & \frac{f_1}{2}+\frac{2n_{\rm l}-1}{4n_{\rm l}}f_2 & 0 & 0 \\
\frac{2n_{\rm l}-1}{4n_{\rm l}}f_2 & \frac{2n_{\rm l}-1}{4n_{\rm l}}f_2 & -\left(\frac{f_1}{4}+\frac{2n_{\rm l}-1}{4n_{\rm l}}f_2\right) & -\frac{f_2}{2} & \frac{f_1}{4}-\frac{f_2}{4n_{\rm l}} & 0 & \frac{f_2}{4n_{\rm l}} & \frac{f_2}{4n_{\rm l}} \\
\frac{2n_{\rm l}-1}{4n_{\rm l}}f_2 & \frac{f_1}{2}+\frac{2n_{\rm l}-1}{4n_{\rm l}}f_2 & -\frac{f_2}{2} & -\left(\frac{f_1}{4}+\frac{2n_{\rm l}-1}{4n_{\rm l}}f_2\right) & 0 & -\left(\frac{f_1}{4}+\frac{f_2}{4n_{\rm l}}\right) & \frac{f_2}{4n_{\rm l}} & \frac{f_2}{4n_{\rm l}} \\
\frac{2n_{\rm l}-1}{4n_{\rm l}}f_2 & -\frac{2n_{\rm l}-1}{4n_{\rm l}}f_2 & \frac{f_1}{4}-\frac{f_2}{4n_{\rm l}} & 0 & -\left(\frac{f_1}{4}+\frac{2n_{\rm l}-1}{4n_{\rm l}}f_2\right) & \frac{f_2}{2} & \frac{f_2}{4n_{\rm l}} & -\frac{f_2}{4n_{\rm l}} \\
-\frac{2n_{\rm l}-1}{4n_{\rm l}}f_2 & \frac{f_1}{2}+\frac{2n_{\rm l}-1}{4n_{\rm l}}f_2 & 0 & -\left(\frac{f_1}{4}+\frac{f_2}{4n_{\rm l}}\right) & \frac{f_2}{2} & -\left(\frac{f_1}{4}+\frac{2n_{\rm l}-1}{4n_{\rm l}}f_2\right) & -\frac{f_2}{4n_{\rm l}} & \frac{f_2}{4n_{\rm l}}
\end{bmatrix},$$

$$[\boldsymbol{K}]_{\rm c} = \begin{bmatrix}
-(f_1+\frac{2n_{\rm l}-1}{2n_{\rm l}}f_2) & 0 & \frac{f_1}{2}+\frac{2n_{\rm l}-1}{4n_{\rm l}}f_2 & -\frac{2n_{\rm l}-1}{4n_{\rm l}}f_2 & \frac{f_1}{2}+\frac{2n_{\rm l}-1}{4n_{\rm l}}f_2 & \frac{2n_{\rm l}-1}{4n_{\rm l}}f_2 & 0 & 0 \\
0 & -\frac{2n_{\rm l}-1}{2n_{\rm l}}f_2 & -\frac{2n_{\rm l}-1}{4n_{\rm l}}f_2 & \frac{2n_{\rm l}-1}{4n_{\rm l}}f_2 & \frac{2n_{\rm l}-1}{4n_{\rm l}}f_2 & \frac{2n_{\rm l}-1}{4n_{\rm l}}f_2 & 0 & 0 \\
\frac{f_1}{2}+\frac{2n_{\rm l}-1}{4n_{\rm l}}f_2 & -\frac{2n_{\rm l}-1}{4n_{\rm l}}f_2 & -\left(\frac{f_1}{4}+\frac{2n_{\rm l}-1}{4n_{\rm l}}f_2\right) & \frac{f_2}{2} & -\left(\frac{f_1}{4}+\frac{f_2}{4n_{\rm l}}\right) & 0 & \frac{f_2}{4n_{\rm l}} & -\frac{f_2}{4n_{\rm l}} \\
-\frac{2n_{\rm l}-1}{4n_{\rm l}}f_2 & \frac{2n_{\rm l}-1}{4n_{\rm l}}f_2 & \frac{f_2}{2} & -\left(\frac{f_1}{4}+\frac{2n_{\rm l}-1}{4n_{\rm l}}f_2\right) & 0 & \frac{f_1}{4}-\frac{f_2}{4n_{\rm l}} & -\frac{f_2}{4n_{\rm l}} & \frac{f_2}{4n_{\rm l}} \\
\frac{f_1}{2}+\frac{2n_{\rm l}-1}{4n_{\rm l}}f_2 & \frac{2n_{\rm l}-1}{4n_{\rm l}}f_2 & -\left(\frac{f_1}{4}+\frac{f_2}{4n_{\rm l}}\right) & 0 & -\left(\frac{f_1}{4}+\frac{2n_{\rm l}-1}{4n_{\rm l}}f_2\right) & -\frac{f_2}{2} & \frac{f_2}{4n_{\rm l}} & \frac{f_2}{4n_{\rm l}} \\
\frac{2n_{\rm l}-1}{4n_{\rm l}}f_2 & \frac{2n_{\rm l}-1}{4n_{\rm l}}f_2 & 0 & \frac{f_1}{4}-\frac{f_2}{4n_{\rm l}} & -\frac{f_2}{2} & -\left(\frac{f_1}{4}+\frac{2n_{\rm l}-1}{4n_{\rm l}}f_2\right) & \frac{f_2}{4n_{\rm l}} & \frac{f_2}{4n_{\rm l}}
\end{bmatrix}.$$

Appendix B: Flow chart of multiscale modeling

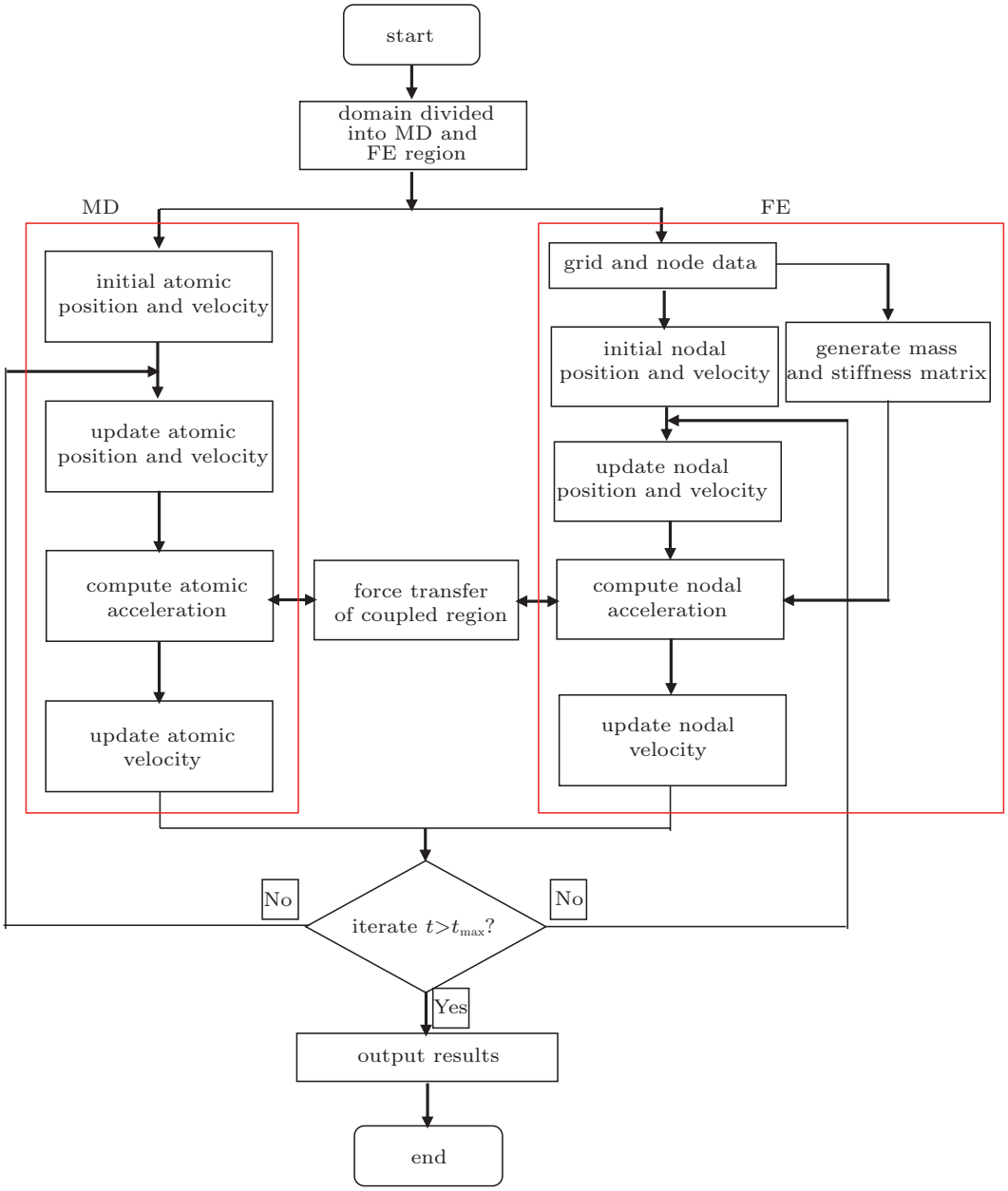


Fig. 11. Flow chart of multiscale modeling.

References

[1] Miller R E and Tadmor E B 2009 *Modell. Simul. Mater Sci. Eng.* **17** 053001
[2] Broughton J Q, Abraham F F, Bernstein N and Kaxiras E 1999 *Phys. Rev. B* **60** 2391
[3] Lidorikis E, Bachlechner M E, Kalia R K, Nakano A and Vashishta P 2001 *Phys. Rev. Lett.* **87** 86104
[4] Tadmor E B, Ortiz M and Phillips R 1996 *Phil. Mag. A* **73** 1529
[5] Shao Y F, Yang X, Zhao X and Wang S Q 2012 *Chin. Phys. B* **21** 093104
[6] Dupuy L M, Tadmor E B, Miller R E and Phillips R 2005 *Phys. Rev. Lett.* **95** 060202
[7] Rudd R E and Broughton J Q 1998 *Phys. Rev. B* **58** R5893
[8] Rudd R E and Broughton J Q 2005 *Phys. Rev. B* **72** 144104
[9] Wanger G J and Liu W K 2003 *J. Comp. Phys.* **190** 249
[10] Xu M, Gracie R and Belytschko T 2010 *Int. J. Numer. Meth. Engng.* **81** 1635
[11] Shilkrot L E, Miller R E and Curtin W A 2002 *Phys. Rev. Lett.* **89** 025501
[12] Warner D H, Curtin W A and Qu S 2007 *Nat. Mater.* **6** 876
[13] Hara S, Kumagai T, Izumi S and Sakai S 2009 *Acta. Mater.* **57** 4209
[14] Luan B Q, Hyun S, Molinari J F, Bernstein N and Robbins M O 2006 *Phys. Rev. B* **74** 46710
[15] Bazant Z P 1978 *Comput. Method. Appl. Mech. Engrg.* **16** 91
[16] Zhou S J, Lomdahl P S, Thomson R and Holian B L 1996 *Phys. Rev. Lett.* **76** 2318
[17] Qu S, Shastry V, Curtin W A and Miller R E 2005 *Modell. Simul. Mater. Sci. Eng.* **13** 1101
[18] Doll J D, Myers L E and Adelman S A 1975 *J. Chem. Phys.* **63** 4908
[19] Cai W, Koning M, Bulatov V V and Yip S 2000 *Phys. Rev. Lett.* **85** 3213
[20] Weinan E and Huang Z 2001 *Phys. Rev. Lett.* **87** 135501
[21] Yang J Z and Li X 2006 *Phys. Rev. B* **73** 224111

[22] Namilae S, Nicholson D M, Nukala P K V V, Gao C Y, Osetsky Y N and Keffer D J 2007 *Phys. Rev. B* **76** 144111
[23] To A C and Li S 2005 *Phys. Rev. B* **72** 035414
[24] Jones R E and Kimmer C J 2010 *Phys. Rev. B* **81** 094301
[25] Bouchbinder E, Fineberg J and Marder M 2010 *Ann. Rev. Cond. Mat.* **1** 371
[26] Sharon E and Fineberg J 1999 *Nature* **397** 333
[27] Ren G, Zhang D and Gong X 2011 *Commun. Comput. Phys.* **10** 1305
[28] Hughes T J R 1987 *The Finite Element Method* (NJ: Prentice- Hall, Englewood Cliffs)
[29] Born M and Huang K 1954 *Dynamical Theories of Cryatal Lattices* (Oxford: Clarendo Press)